Journal of Hazardous Materials 514 (2026) 142782

Contents lists available at ScienceDirect

Journal of Hazardous Materials

journal homepage: www.elsevier.com/locate/jhazmat

Highly synergistic degradation of fluoroquinolones driven by redox dual channel mechanism in Fe(III)-mediated thermally activated persulfate system

Lingzhi Shen [a], Yongpeng Zhang [a], Yuxing Xian [a], Zihong Xu [a], Zihao Guo [a], Yixun Zheng [a], Yue Yang [a], Zili Lin [b,c], Kun Yao [a,*], Zheng Hu [a], Yanli Wang [a], Zhenjun Xiao [a], Ping Chen [a,*], Wenying Lv [a], Guoguang Liu [a]

[a] Guangdong Key Laboratory of Environmental Catalysis and Health Risk Control, School of Environmental Science and Engineering, Institute of Environmental Health and Pollution Control, Guangdong University of Technology, Guangzhou 510006, China
[b] School of Marine Science and Technology, Shanwei Institute of Technology, Shanwei 516600, China
[c] Shanwei Marine Industry Institute, Shanwei 516600, China

HIGHLIGHTS

- Fe(III) and heat exhibit strong synergy triggered at a low temperature of 40 °C.
- Activation energy is reduced from 89.58 to 18.53 kJ/mol by Fe(III) mediation.
- A redox dual channel mechanism is established with $O_2^{\bullet-}$ as the key reductant.
- The system shows robust real-water performance.

GRAPHICAL ABSTRACT

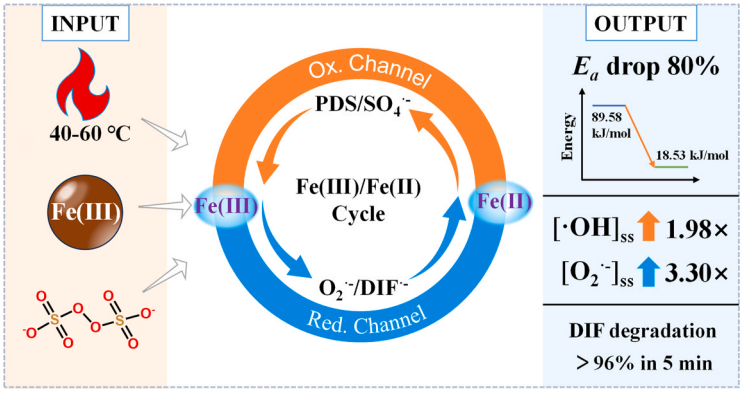

ARTICLE INFO

Keywords:
Thermally activated peroxydisulfate
Fe(III)/Fe(II) cycle
Redox dual channel mechanism
Reactive species
Fluoroquinolone antibiotics

ABSTRACT

The thermally activated peroxydisulfate (heat/PDS) system for water treatment suffers from a single reaction pathway and high energy consumption. This study investigates the regulatory role of Fe(III) in the heat/PDS system using difloxacin (DIF) as a target. Fe(III) acts as a redox mediator, reducing the activation energy from 89.58 kJ/mol in heat/PDS alone to 18.53 kJ/mol. The synergy of Fe(III) and heat is triggered at 40 ℃, a temperature naturally attainable in sun-warmed surface waters or from low-grade waste heat. At this temperature, the synergy enhances the DIF degradation rate constant by 20.30 and 5.67 times compared to the heat/PDS and Fe(III)/PDS systems alone. When raising to 60 ℃, a level readily accessible using industrial waste heat or concentrated solar energy, the system achieves even faster kinetics. The steady-state concentration of hydroxyl radical (•OH) reaches 4.16×10^{-12} M, which is 1.98 times that of the heat/PDS system. Mechanistically, Fe(III)

* Corresponding authors.
E-mail addresses: yaokun@gdut.edu.cn (K. Yao), koala@gdut.edu.cn (P. Chen).

https://doi.org/10.1016/j.jhazmat.2026.142782
Received 10 May 2026; Received in revised form 10 June 2026; Accepted 20 June 2026
Available online 24 June 2026

forms $Fe(DIF^{\pm})^{3+}$ complexes that facilitate interfacial electron transfer and accelerate the Fe(III)/Fe(II) cycle. Within this cycle, superoxide radicals ($O_2^{\bullet-}$) act as a reducing agent to efficiently regenerate Fe(II), while PDS and sulfate radicals ($SO_4^{\bullet-}$) serve as oxidants to drive the cycle and generate high-valent iron-oxo species (Fe(IV)=O). This redox dual channel mechanism centered on the Fe(III)/Fe(II) cycle significantly enhances DIF degradation. The system exhibits pH-dependent activity (optimal at pH 3.5) and strong real-water robustness. This work provides a theoretical foundation for utilizing abundant iron ions with low grade heat to treat antibiotic polluted water.

1. Introduction

Fluoroquinolone antibiotics (FQs) are widely used but poorly metabolized, with ~70% of the parent drug excreted into the environment [1,2]. It is reported that FQs concentration reach 1990 ng/L in Chinese aquaculture waters, and even mg/L levels in pharmaceutical wastewater [3–6]. Difloxacin (DIF), a typical FQ featuring a difluoro-substituted structure and zwitterionic character (carboxyl $pK_{a1} = 5.91$, piperazine ring $pK_{a2} = 9.89$), is barely removed by conventional water treatment processes [7,8]. Residual DIF in the environment not only potentially induces the emergence and spread of bacterial resistance but also poses carcinogenic, teratogenic, and endocrine-disrupting risks to aquatic organisms [9–11]. Developing treatment technologies capable of achieving deep DIF removal is therefore of considerable practical significance.

Persulfate-based advanced oxidation processes (PS-AOPs) have attracted extensive attention for removing refractory organic pollutants, primarily because the $SO_4^{\bullet-}$ generated possesses a high redox potential (2.5–3.1 V) and a relatively long half-life (30–40 μs) [12–14]. Among various activation methods, thermally activated peroxydisulfate (heat/PDS) has emerged as a research focus owing to its operational simplicity, system homogeneity, and freedom from external catalysts [15,16]. However, our previous work and other studies have revealed that the heat/PDS system alone suffers from intrinsic limitations including a relatively singular reaction pathway, high energy consumption, and suboptimal radical utilization efficiency [7,17]. Introducing naturally coexisting constituents to overcome these bottlenecks represents a critical challenge for the practical application of this technology.

Iron is the fourth most abundant element in the Earth's crust and is widely distributed in various aquatic environments [18–20]. Fe(III), as the most stable oxidation state under aerobic conditions, is ubiquitous in surface waters and sediments. In practical environmental scenarios, such as sun-warmed surface waters or industrial wastewater discharge zones, the coexistence of Fe(III) and thermal energy is a common phenomenon [21]. This ubiquity positions Fe(III) as a potential natural mediator in thermally driven oxidative processes [22–24]. However, while previous studies have extensively explored the use of exogenous zero-valent iron or Fe(II) for persulfate activation [25], the regulatory role of endogenous or environmentally prevalent Fe(III) in heat-activated systems, especially its ability to lower energy barriers and alter reaction pathways, remains insufficiently explored.

Our earlier work showed that Cu(II) induces a radical pathway switch via Cu(III) intermediates, shifting the dominant species from $SO_4^{\bullet-}$ to •OH [26]. This revealed metal ions as pathway regulators, not just activator. However, whether this switching mechanism applies beyond Cu(II) is unclear. Fe(III), with geochemical behavior distinct from Cu(II), may follow different regulatory patterns. Fe(III) has a stronger hydrolysis tendency, broader species distribution (soluble under acidic conditions, precipitating near neutral pH [27]), and lower redox potential (Fe(III)/Fe(II), $E^{\circ} = 0.77$ V) than Cu(II)/Cu(III) [28]. These differences suggest fundamentally distinct activation pathways. In addition, $O_2^{\bullet-}$ forms in situ during PDS activation [29,30], could it drive the Fe(III)/Fe(II) cycle as a reducing agent? Also, is high-valent iron (e.g., Fe(IV)=O) generated? Answering these questions would advance understanding of metal-specific regulation in heat/metal/PDS systems and potentially clarify the redox dual channel mechanism.

Accordingly, this study adopts DIF as the target pollutant and constructs a ternary heat/Fe(III)/PDS system to systematically investigate the regulatory role and mechanism of Fe(III) in thermally activated PDS processes. The specific objectives are as follows: (1) Elucidating the Fe(III)-mediated E_a evolution and synergistic factors during DIF degradation; (2) Identifying and quantifying the reactive species ($SO_4^{\bullet-}$, •OH, $O_2^{\bullet-}$, and Fe(IV)=O) and assessing their relative contributions; (3) Revealing the intrinsic mechanism by which the $Fe(DIF^{\pm})^{3+}$ complexes facilitate interfacial electron transfer and accelerates the Fe(III)/Fe(II) cycle, and elucidating the principle by which PDS and $SO_4^{\bullet-}$ (oxidative channel) operate in concert with $O_2^{\bullet-}$ (reductive channel) to construct a multi-component synergistic oxidation network; (4) Evaluating the effects of coexisting anions (Cl^-, HCO_3^-, NO_3^-, etc.), humic acid (HA), real water matrices and different metal ions on degradation performance, thereby providing a theoretical foundation for developing low-carbon, high-efficiency water treatment technologies utilizing environmentally abundant iron ions.

2. Materials and methods

2.1. Reagents and experimental procedures

All chemical reagents utilized throughout this research were of analytical grade or higher purity. Detailed information regarding these materials is provided in Text S1 of the Supplementary Material. The DIF degradation experiments in wastewater were simulated in a magnetically stirred constant-temperature system (50 mL, $[DIF]_0 = 10$ mg/L, [PDS] = 2 mM, 25–60 °C, pH 3.5 or 6.5). Fe(III), Co(II), Mn(II), and Cr(III) were added at 17.9 μM as sulfate or nitrate salts. Reactions were terminated with excess $Na_2S_2O_3$ (500 mM). Detailed conditions are provided in Text S2.

2.2. Qualitative and quantitative analysis of reactive species

•OH, $SO_4^{\bullet-}$, and $O_2^{\bullet-}$ were detected by electron paramagnetic resonance (EPR, Bruker EMXplus, Germany) using 5,5-dimethyl−1-pyrroline N-oxide (DMPO) as spin trap, and $^1O_2$ using 2,2,6,6-tetramethylpiperidine (TEMP). Quenching experiments were conducted by using MeOH (500 mM, for •OH and $SO_4^{\bullet-}$), TBA (500 mM, for •OH), and TEMPO (20 mM, for $O_2^{\bullet-}$) [31,32]. Apparent contributions were calculated according to Text S3. Steady-state concentrations of •OH and $SO_4^{\bullet-}$ were determined using nitrobenzene (NB) and anisole (AS) probes with temperature-corrected rate constants [26]. $O_2^{\bullet-}$ was quantified using the 4-chloro−7-nitrobenzo−2-oxa−1,3-diazole (NBD-Cl) fluorescence method [33]. Fe(IV)=O was probed by methyl phenyl sulfoxide (PMSO) oxidation, with methyl phenyl sulfone ($PMSO_2$) quantified by high-performance liquid chromatography (HPLC, Shimadzu, Japan) (Text S4 and Table S1). $SO_4^{\bullet-}$ was monitored at 450 nm by laser flash photolysis (LKS80, applied light physics, UK; Text S3).

2.3. Complexation and electrochemical analysis

Fe(III)-DIF complexes were characterized by UV-Vis spectroscopy (200–550 nm, UV3200, Shanghai Mapada Instruments Co., LTD., China;

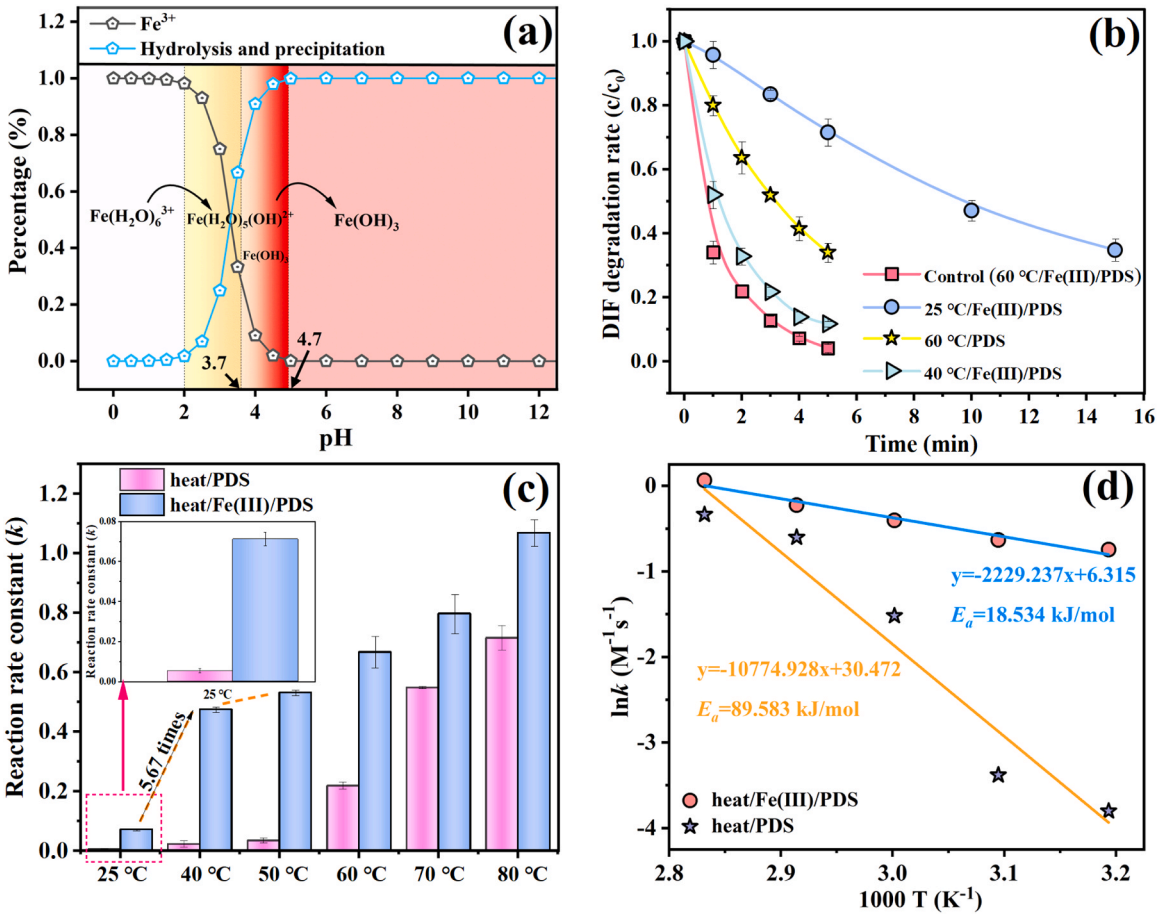

Fig. 1. (a) Speciation distribution of Fe(III) under different pH conditions; (b) Degradation analysis of DIF by the heat/Fe(III)/PDS system at different temperatures; (c) Comparison of DIF degradation rates in the binary system (heat/PDS and 25 ℃/Fe(III)/PDS) and the ternary heat/Fe(III)/PDS system at different temperatures; (d) Effect of Fe(III) addition on the E_a of heat/PDS (general conditions in this study: The pH for the activity study was set at 3.5, [Fe(III) or other metal ions] = 17.9 μM, T = 60 ℃, [PDS] = 2 mM, [DIF] = 10 mg/L, and error bars represent one standard deviation).

Text S4). Electron transfer was evaluated by chronoamperometry (CHI760E, Shanghai Chenhua Instrument Co., LTD., China). Fe(II) concentration was measured by the 1,10-phenanthroline method (Text S5 and Fig. S1) [34]. Mechanistic evaluation of metal ion-mediated influence can be seen from Text S6.

2.4. Theoretical computational methods

DFT calculations were performed using the PBE functional under GGA with a DNP basis set and a global orbital cutoff radius of 3.500 Å [35,36]. The convergence tolerance was set to 1×10^{-5} Hartree with a maximum of 500 SCF cycles, and vibrational frequency analysis was conducted to confirm stable configurations and obtain Gibbs free energies (detailed conditions provided in Text S7).

3. Results and discussion

3.1. Activity of the heat/Fe(III)/PDS system

The ability of Fe(III) to activate PDS is strongly dependent on solution pH due to its hydrolysis speciation (Fig. 1a). Fe(III) remains predominantly soluble under acidic conditions (pH < 3.5) but gradually precipitates as hydroxides when the pH rises to near neutral [27]. To systematically evaluate this pH-dependent activation behavior, two representative conditions, pH 3.5 and pH 6.5, were selected for subsequent experiments, thereby effectively simulating reaction scenarios in acidic and circumneutral water qualities.

At pH 3.5 (Fig. S2), PDS alone, heat alone, and heat/Fe(III) showed negligible DIF degradation. The Fe(III)/PDS system achieved 28.5% removal at 25 °C within 5 min (65.2% at 15 min, Fig. 1b), consistent with Caiet al [24]. Raising the temperature to 40 °C dramatically increased degradation to 88.3% within 5 min (Fig. 1c). The synergy enhances the DIF degradation rate constant by 20.30 and 5.67 times compared to the heat/PDS and Fe(III)/PDS systems alone. This suggests that a shift in radical generation pathways at low temperatures. Notably, ~40 ℃ is naturally attainable in summer surface waters or from low-grade waste heat. [21], suggesting potential for solar-driven, low--carbon treatment. When the temperature reaches 60 ℃, a common threshold for utilizing industrial waste heat, the rate constant of the Fe (III)-mediated system is 40.6% higher than that of the Fe(III)/PDS system at 40 ℃. Even beyond this temperature threshold where the synergistic burst is already triggered, Fe(III) continues to facilitate the reaction by dramatically reducing the activation energy (E_a) of the heat/PDS system from 89.58 kJ/mol to 18.53 kJ/mol, highlighting that Fe(III) serves as an efficient redox mediator that bridges thermal energy and persulfate activation (Fig. 1d). Consequently, the results at both temperatures underscore the broad adaptability and high efficiency of this technology. Further temperature increases progressively accelerated the degradation, with rate constants of 0.800 min^{-1} and 1.068 min^{-1} at 70 and 80 °C, respectively. In addition, compared to the two binary systems, the ternary synergistic factors calculated via Eq.1 and data of Fig. 1c are 5.08, 5.05, 2.31, 1.29, and 1.36 across the range of 40–80 ℃, further indicating the synergy of heat and Fe(III). Moreover, the synergistic factor decreases from ≥ 2.31 at 40–60 ℃ to near unity at

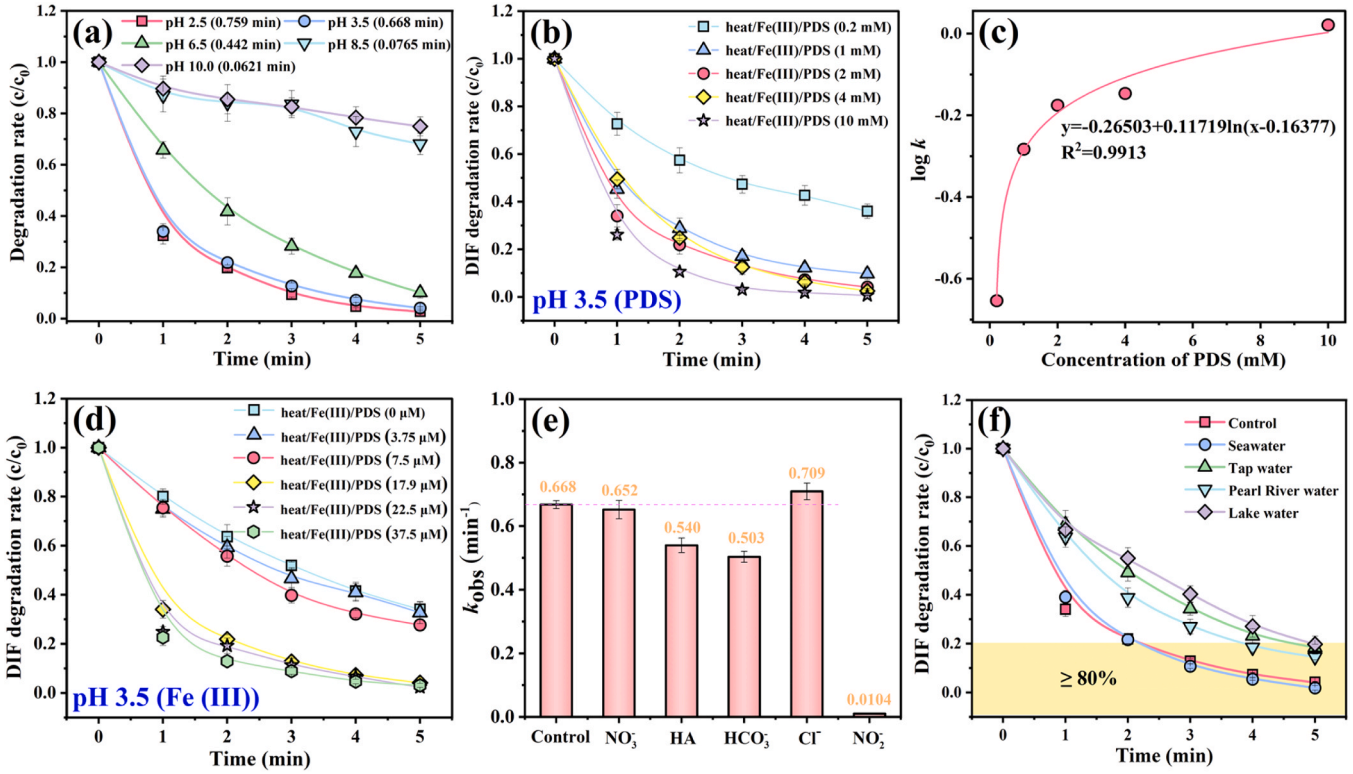

Fig. 2. Effect of pH (a) and PDS (b) on DIF degradation in the heat/Fe(III)/PDS system; (c) Fitting curve of DIF degradation rate constant (log k) versus PDS concentration; (d) Effect of Fe(III) concentration on DIF degradation in the heat/Fe(III)/PDS system; Effects of different environmental factors (e) and water matrices (f) on the degradation rate constant of DIF in the heat/Fe(III)/PDS system.

70–80 ℃, indicating that Fe(III)-mediated activation dominates at low to medium temperatures, whereas direct thermal activation of PDS becomes increasingly important at higher temperatures. To balance energy conservation with efficiency, subsequent investigations focused on 25, 40, and 60 ℃.

$$SF_{heat/Fe(III)/PDS} = \frac{k_{heat/Fe(III)/PDS}}{k_{heat/PDS} + k_{Fe(III)/PDS}} \quad (1)$$

Where $k_{Fe(III)/PDS}$, $k_{heat/PDS}$ and $k_{heat/Fe(III)/PDS}$ represent the rate constants for the binary and ternary systems (Fig. 1c data), respectively.

The initial pH of the solution significantly influenced the DIF degradation efficiency in the heat/Fe(III)/PDS system (Fig. 2a). The highest degradation rate was achieved at an initial pH of 2.5–3.5, while a sharp decline in performance was observed as the pH increased from 6.5 to 10. This pH-dependent behavior reflects a trade-off between the speciation of the pollutant and the metal ion. On one hand, as the pH approaches the near-neutral range, the deprotonation of DIF (carboxyl $pK_{a1} = 5.91$, piperazine ring $pK_{a2} = 9.89$) increases its electron density, which theoretically enhances its reactivity toward electrophilic radicals [37,38]. However, the speciation of Fe(III) remains the dominant factor governing the overall system activity. At pH 3.5, Fe(III) exists primarily in highly active soluble forms [27,39], which effectively mediate the redox cycles for PDS activation. In addition, only minor pH fluctuations (within ±0.4 units) were observed before and after the reaction (Fig. S3a). As the pH increases, the rapid hydrolysis and precipitation of iron species (forming $Fe(OH)_3$) drastically reduce the concentration of available activated centers, thereby suppressing the synergistic effect. The rate constant ratio of the ternary system to heat/PDS alone decreases from 3.05 at pH 3.5–1.95 at pH 6.5, indicating that the heat/Fe(III) synergy is stronger under acidic conditions, whereas the heat/PDS pathway becomes more important under neutral conditions.

As the precursor of reactive species, the PDS concentration directly governs the total yield of various radicals. In Fig. 2b, an increase in PDS concentration from 0.2 to 2 mM, at pH 3.5 and 60 ℃, leads to a progressive enhancement in the DIF degradation rate within the heat/Fe(III)/PDS system, achieving approximately 96% removal at 2 mM. The relationship between the PDS concentration and log k was fitted to the equation $y = -0.26503 + 0.11719ln(x-0.16377)$, demonstrating a strong positive correlation with an R^2 value of 0.9913 (Fig. 2c). The fitted curve identifies the 1–2 mM range as a distinct inflection region representing the optimal concentration plateau, beyond which the curve flattens. This observed saturation in degradation rates at higher PDS dosages may be attributed to self-quenching reactions between excess PDS and active radicals (Eq. 2) [40]. Regarding Fe(III), its concentration directly dictates the PDS activation efficiency and the specific pathways of radical generation. Fig. 2d demonstrates that with a fixed PDS concentration of 2 mM, the DIF degradation efficiency within 5 min improves as the Fe(III) concentration rises from 0 μM to 37.5 μM, reaching values of 66.0–96.3%. These results indicate that the introduction of Fe(III) substantially enhances the oxidative capacity of the system through its synergistic interaction with thermal activation. When the Fe(III) dosage exceeds approximately 17.9 μM, the incremental increase in the degradation rate slows markedly, indicating that Fe(III)-mediated reactivity reaches a plateau. Considering both activation efficiency and economic feasibility, a Fe(III) concentration of 17.9 μM (approximately 1 mg/L) was selected as the baseline condition for subsequent studies, as this value aligns with Fe(III) levels typically found in actual wastewater.

$$SO_4^{\bullet-} + S_2O_8^{2-} \xrightarrow{heat} S_2O_8^{\bullet-} + SO_4^{2-} \quad (2)$$

Furthermore, under the conditions of pH 3.5 and 60 ℃, the ternary heat/Fe(III)/PDS system was utilized to degrade various FQs. As illustrated in Fig. S3b, the system exhibited excellent degradation performance for all five FQs within a 5-minute interval, achieving removal efficiencies of 95.9%, 74.6%, 93.5%, 84.0%, and 70.4% for DIF, lomefloxacin (LOM), enrofloxacin (ENR), ciprofloxacin (CIP), and ofloxacin (OFX), respectively, demonstrating the robust capacity and broad

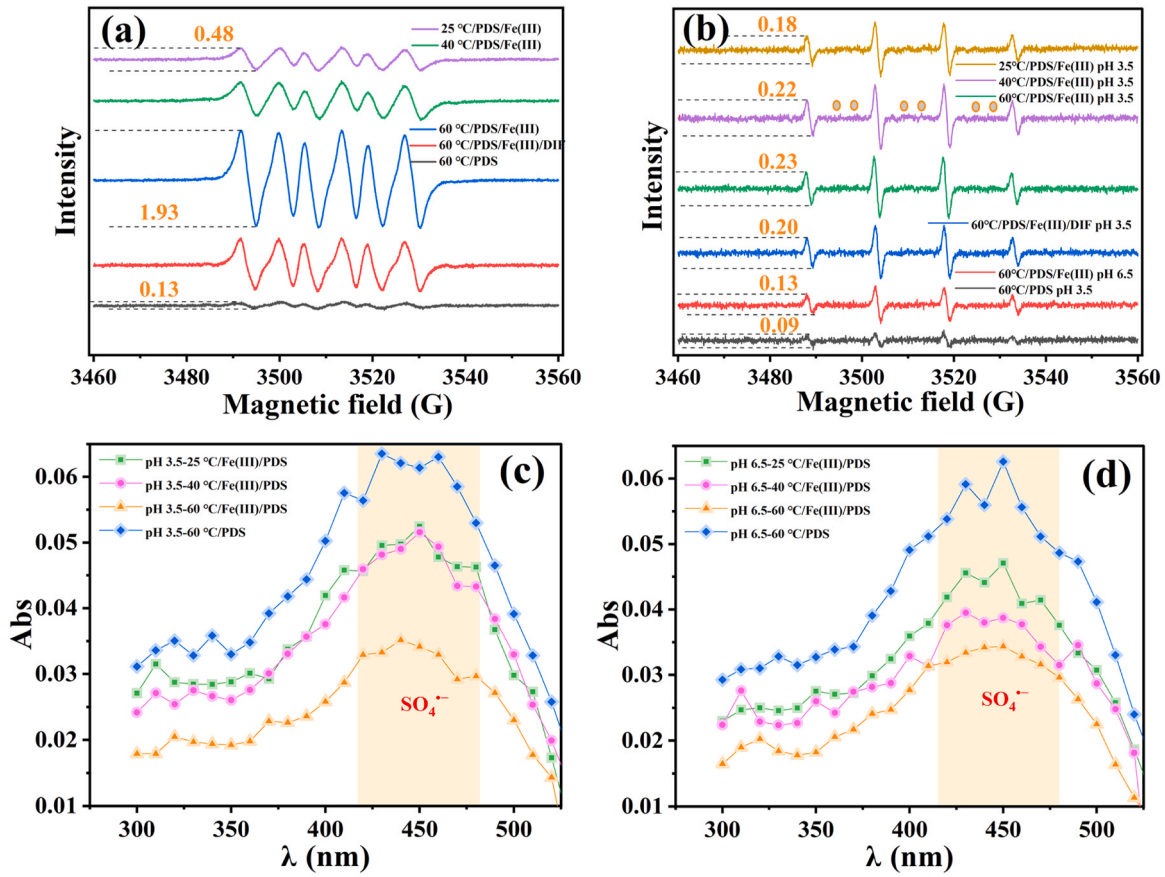

Fig. 3. (a) Comparison of EPR signal intensities of $O_2^{\bullet-}$ in different systems (using DMPO as spin trap in methanol solution, 70.5 mM); (b) EPR spectra of •OH and $SO_4^{\bullet-}$ in different systems (using DMPO as spin trap in aqueous solution, 70.5 mM); Generation kinetics of $SO_4^{\bullet-}$ in heat/PDS and heat/Fe(III)/PDS systems under (c) pH 3.5 and (d) pH 6.5 condition measured by laser flash photolysis (λ = 450 nm; data represents absolute absorbance).

applicability of this system for FQs treatment.

3.2. Environmental adaptability of the heat/Fe(III)/PDS system

The impact of ubiquitous HA and inorganic anions including NO_3^-, HCO_3^-, Cl^- and NO_2^- on DIF degradation was systematic evaluated to assess the practical applicability of the heat/Fe(III)/PDS system. As shown in Fig. 2e, the presence of NO_3^- and Cl^- had weak effects on the reaction kinetics. Their respective k_{obs} values were 0.652 min^{-1} and 0.709 min^{-1}, representing a 2.4% inhibition and a 6.1% promotion. Cl^- may slightly facilitate radical regeneration (e.g. $Cl^{\bullet}$) or transfer through subtle radical chain reactions [41,42]. The addition of HA resulted in a moderate inhibitory effect, with k_{obs} decreasing to 0.540 min^{-1} and an inhibition rate of 19.2%. This reduction is primarily attributed to the role of HA as a representative dissolved organic matter containing abundant aromatic structures and unsaturated bonds. HA can reduce the activity of metal ions through complexation, and also scavenges $SO_4^{\bullet-}$ and •OH, thereby hindering the degradation of DIF. Similarly, the presence of HCO_3^- led to a moderate decrease in activity, likely due to the scavenging of $SO_4^{\bullet-}$ and •OH [43,44], and the subsequent increase in solution pH, which promotes the precipitation of Fe(III) hydroxides.

The most profound inhibitory effect was observed with NO_2^-, where k_{obs} plummeted to 0.0104 min^{-1}, corresponding to an inhibition rate of 98.4%. NO_2^- functions not only as a strongly reducing anion that terminates the effective Fe(III)/Fe(II) cycle but also undergoes rapid electron transfer with $SO_4^{\bullet-}$ (Eq. 3) with a second-order rate constant of 8.8×10^8 $M^{-1}s^{-1}$. This reaction generates low-activity nitrite radicals ($NO_2^{\bullet}$) and almost entirely quenches the oxidative capacity of the system [45]. This outcome suggests that pretreatment or increased oxidant dosage is necessary when treating wastewater containing NO_2^-.

$$NO_3^- + SO_4^{\bullet-} \rightarrow NO_2^{\bullet} + SO_4^{2-}, \quad k = 8.8\times 10^8 M^{-1}S^{-1} \tag{3}$$

To assess practical applicability, DIF degradation was evaluated in various real-world water matrices (Fig. 2f). In tap water, the degradation rate was 81.6%, representing a decrease of 14.3 %age points compared to the control. Similarly, the degradation rates in Pearl River water and lake water were 85.5% and 80.2%, reflecting reductions of 10.4 and 15.7 %age points, respectively. Correlating these findings with water quality parameters (Table S2), the inhibitory effects are primarily attributed to higher concentrations of total organic carbon (TOC) and HCO_3^-. Conversely, seawater achieved 98.1% degradation, a 2.2% increase over the control. Despite containing TOC and HCO_3^-, the high Cl^- concentration (21.43 mg/L) in seawater effectively offset their inhibitory effects, leading to an overall promotion [46]. Additionally, the abundance of diverse ions in seawater, including Br^-, Mg^{2+}, and Ca^{2+}, may exert a composite effect [47], facilitating the Fe(III)/Fe(II) cycle to maintain a continuous generation of reactive species. In summary, while most real-world water matrices exhibit a degree of inhibition except for the slight promotion in seawater, the degradation rates consistently remained above 80% at 5 min. This performance underscores the tolerance and application potential of the system when treating complex water environments.

3.3. Qualitative and quantitative analysis of reactive species in the heat/Fe(III)/PDS system

3.3.1. Qualitative characterization via EPR and laser flash photolysis

To elucidate the regulatory role of Fe(III) on the generation of

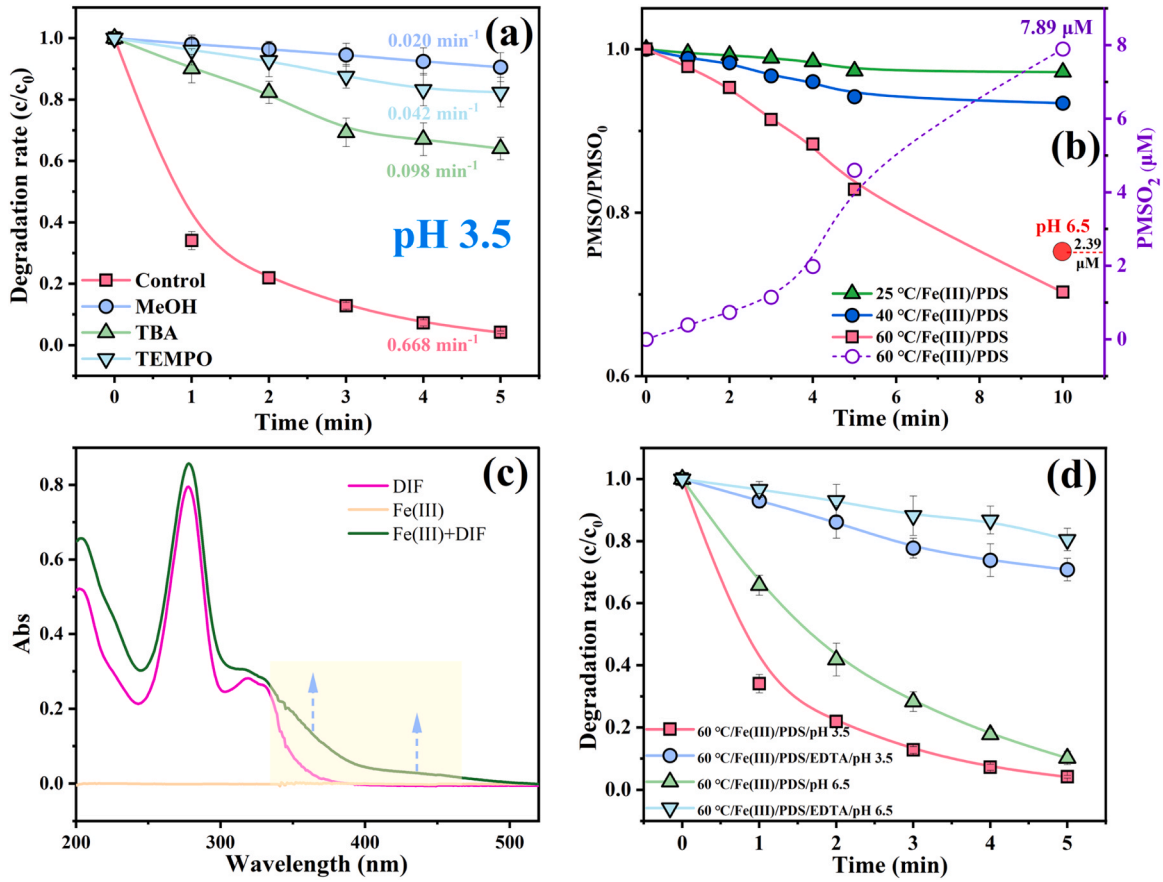

Fig. 4. (a) Inhibitory effects of TBA (500 mM), MeOH (500 mM), and TEMPO (20 mM) on the activity of the heat/Fe(III)/PDS system at pH 3.5; (b) Verification experiment for high-valent iron-oxo species (Fe(IV)=O) in the heat/Fe(III)/PDS system; Complexation between Fe(III) and DIF and its effect on DIF degradation, (c) UV-Vis absorption spectra of the Fe(III)-DIF complexes and (d) inhibitory effect of EDTA.

reactive species within the thermally activated PDS system, this study first performed qualitative and semi-quantitative analyses of potential key species including $^1O_2$, $O_2^{\bullet-}$, •OH and $SO_4^{\bullet-}$ using EPR technology. As illustrated in Fig. S4, with TEMP employed as the trapping agent at pH 3.5 and pH 6.5, no significant TEMP-$^1O_2$ characteristic signals was detected. Thus $^1O_2$ is not a primary reactive species in homogeneous thermally activated PDS systems, likely due to insufficient PDS hydrolysis products or rapid quenching [48].

The generation of $O_2^{\bullet-}$ was monitored in a methanol solvent using DMPO as the trapping agent, with the results presented in Fig. 3a. The data reveal substantial variations in $O_2^{\bullet-}$ signal intensities across different systems. In the 60 °C/PDS system, the $O_2^{\bullet-}$ signal intensity, determined by the height of the leftmost peak for semi-quantitative comparison, was only 0.13. This indicates a weak capacity for individual thermal activation of PDS to produce $O_2^{\bullet-}$, which aligns with the findings of Yang et a [45]. In the Fe(III)/PDS system at 25 ℃, the signal intensity reached 0.48, approximately 3.7 times that of the heat/PDS system, demonstrating that the introduction of Fe(III) effectively promotes $O_2^{\bullet-}$ generation [22]. In the heat/Fe(III)/PDS system, the $O_2^{\bullet-}$ signal intensity increased with rising temperature, reaching 0.68 at 40 °C and 1.93 at 60 ℃. The intensity at 60 ℃ was 4.0 times that of the ambient Fe(III)/PDS system, 2.8 times that of the 40 ℃ system, and 14.8 times that of the 60 °C/PDS system. These findings confirm that the synergy between Fe(III) and thermal activation enhances $O_2^{\bullet-}$ production. Furthermore, the addition of the target pollutant DIF led to a notable reduction in the $O_2^{\bullet-}$ signal, with the intensity in the 60 ℃/Fe(III)/PDS/DIF system dropping to 1.03. This phenomenon highlights that $O_2^{\bullet-}$ either directly participates in DIF degradation or indirectly facilitates DIF removal by mediating the generation of other reactive species such as $SO_4^{\bullet-}$ and •OH, thereby validating its critical role within the reaction framework [29].

The generation of •OH and $SO_4^{\bullet-}$ was further investigated using DMPO as the spin trapper, as shown in Fig. 3b. At pH 3.5, the radical signal intensities varied among the systems. For 25 ℃, the Fe(III)/PDS system exhibited characteristic DMPO-•OH quartet signals with a 1:2:2:1 intensity ratio alongside weak DMPO-$SO_4^{\bullet-}$ signals. The $SO_4^{\bullet-}$ signals remained consistently weak and difficult to identify clearly. This observation is likely due to the rapid conversion of $SO_4^{\bullet-}$ to •OH via hydrolysis or reaction with H_2O/OH^- in aqueous systems (Eq. 4), a process accelerated by heat that results in extremely low steady-state concentrations of $SO_4^{\bullet-}$. The •OH signal intensity was approximately 0.18, suggesting that Fe(III) possesses an inherent capacity to activate PDS and induce radical formation. Upon increasing the temperature to 60 °C, the •OH signal intensity in the heat/Fe(III)/PDS system rose to 0.23, roughly 1.28 times the ambient level, demonstrating that elevated temperatures enhance the activation of PDS by Fe(III) [49].

Compared to the binary 60 ℃/PDS system which yielded a •OH signal of 0.09, the 60 ℃/Fe(III)/PDS system achieved a signal intensity of 0.23, representing a 2.56-fold increase. This confirms that the synergy between Fe(III) and heat bolsters radical generation. Following the addition of DIF, the •OH signal intensity decreased slightly, indicating its involvement in the degradation process. However, the minor extent of this decrease suggests that the •OH generation rate effectively offsets its consumption, maintaining an ample radical supply and high steady-state concentrations of reactive species. Regarding the influence of pH, the •OH signal intensity in the 60 ℃/Fe(III)/PDS system at pH 3.5 (0.23) was 1.77 times stronger than that at pH 6.5 (0.13), which is consistent with the degradation kinetic trends observed in Section 3.1. In acidic

environments, Fe(III) exists primarily as soluble ions which are more conducive to activating PDS through complexation or electron transfer mechanisms, thereby promoting radical chain reactions. Conversely, at pH 6.5, Fe(III) tends to form poorly ionized hydroxides, which reduces its catalytic activity and diminishes radical generation.

$$SO_4^{\bullet-} + OH^- \leftrightarrow \bullet OH + SO_4^{2-}, k = 6.5 \times 10^7 \quad M^{-1}s^{-1} \tag{4}$$

Since EPR failed to provide a distinct signal for $SO_4^{\bullet-}$, rendering it difficult to directly elucidate the synergistic mechanism between Fe(III) and thermal activation, this study employed laser flash photolysis to monitor transient absorption signals at 450 nm, the characteristic absorption wavelength of $SO_4^{\bullet-}$. The results are illustrated in Fig. 3c-d. At pH 3.5, the investigation initially focused on the heat/PDS system (60 ℃) without Fe(III) supplementation. This system exhibited the highest absorbance at 450 nm among all tested conditions, indicating that thermal activation effectively induces PDS decomposition to generate substantial concentrations of $SO_4^{\bullet-}$ as described in Eq. 5. However, the introduction of Fe(III) resulted in a consistent decline in absorbance. Specifically, the absorbance values for the Fe(III)-containing systems at 25 ℃, 40 ℃, and 60 ℃ decreased sequentially and remained lower than those of the corresponding systems lacking Fe(III) at identical temperatures. This trend suggests that while the synergy between Fe(III) and heat enhances overall PDS activation efficiency, the steady-state concentration of $SO_4^{\bullet-}$ decreases with increasing temperature. Correlating this with the EPR results, where •OH signals intensified at higher temperatures, it can be inferred that elevated temperatures facilitate the transformation of $SO_4^{\bullet-}$ into •OH as shown in Eq. 4. This observation confirms the dynamic transformation mechanism of radical species within the heat/Fe(III)/PDS system. Under pH 6.5 conditions (Fig. 3d), the overall absorbance values were slightly lower than those at pH 3.5, which is consistent with the reduced activity of Fe(III) as it primarily exists in hydroxide forms in circumneutral environments. Nevertheless, the Fe(III)-containing systems demonstrated a similar pattern to the pH 3.5 systems, with absorbance decreasing as temperature rose. This phenomenon further supports the conclusion that thermal activation drives the rapid conversion of excess $SO_4^{\bullet-}$ into •OH in the presence of Fe (III). The remaining $SO_4^{\bullet-}$ that has not undergone complete transformation, evidenced by the absorbance at 450 nm in the ternary system remaining near 0.035 in Fig. 3c, works in tandem with •OH to efficiently attack DIF molecules. This synergistic effect leads to more thorough degradation, thereby enhancing overall oxidation efficiency while simultaneously reducing the steady-state concentration of $SO_4^{\bullet-}$.

$$S_2O_8^{2-} \xrightarrow{\Delta} 2SO_4^{\bullet-}, k = 5.7 \times 10^{-5}s^{-1} \tag{5}$$

3.3.2. Qualitative and semi-quantitative analysis via chemical competition experiments

Under the condition of pH 3.5 (Fig. 4a), the addition of TBA for •OH scavenging (detailed in Section 2.2) caused the degradation rate constant (k) to decrease substantially from 0.668 min^{-1} to 0.098 min^{-1}. Upon the introduction of MeOH to scavenge both •OH and $SO_4^{\bullet-}$, k further declined to 0.020 min^{-1}. Calculations based on Eq. S1 and S2 reveal that the apparent contributions of •OH and $SO_4^{\bullet-}$ are 85.3% and 11.7%, respectively. These values contrast sharply with the results of the standalone heat/PDS system under similar conditions, which exhibited contributions of 75.3% for •OH and 20.1% for $SO_4^{\bullet-}$ (Fig. S5a). The incorporation of Fe(III) resulted in a nearly 10% increase in the •OH contribution and a corresponding 8% reduction in the $SO_4^{\bullet-}$ contribution, suggesting that Fe(III) shifts the equilibrium of radical generation and transformation to strengthen the dominance of •OH. At pH 6.5 (Fig. S6), the addition of TBA and MeOH reduced the k values by 83.5% and 93.2%, respectively. The contributions of the two radicals were similar to those observed at low pH. Notably, the addition of TEMPO as an $O_2^{\bullet-}$ scavenger inhibited DIF degradation at both pH levels. This inhibition was markedly more pronounced than the degradation effect attributed to $O_2^{\bullet-}$ in the standalone heat/PDS system (Fig. S5b). It should be noted that TEMPO is not a fully selective scavenger for $O_2^{\bullet-}$ and may also react with •OH; therefore, the inhibition observed upon TEMPO addition should be interpreted with caution. However, complementary evidence from EPR experiments consistently supports the involvement of $O_2^{\bullet-}$ in the system.

These results corroborate the data obtained from EPR and laser flash photolysis, forming a consistent evidence chain. Specifically, the enhanced •OH signals observed in EPR upon Fe(III) addition and the attenuation of the characteristic $SO_4^{\bullet-}$ absorption peaks in flash photolysis support the semi-quantitative shifts identified in the scavenging experiments. Collectively, this evidence indicates that Fe(III) acts not only as an activator to increase the overall reaction rate but also as a regulator that shifts the primary reactive species from $SO_4^{\bullet-}$ to •OH. This shift becomes more significant with increasing temperature. Furthermore, the accompanying electron transfer processes generate substantial amounts of $O_2^{\bullet-}$, driving a secondary reaction network for more efficient DIF degradation. This is supported by previous reports from Keenan et al. [50] regarding secondary mechanisms where $O_2^{\bullet-}$ participates in the generation of H_2O_2 and •OH [51].

To verify the existence of Fe(IV)=O within the heat/Fe(III)/PDS system, PMSO was employed as a specific probe [51]. The results demonstrate effective PMSO degradation at pH 3.5 across various temperatures including 25, 40, and 60 ℃. Although •OH can oxidize PMSO through multiple pathways such as those shown in Eq. 6, it does not produce the characteristic oxidation product $PMSO_2$[52–54]. In this study, significant $PMSO_2$ formation was detected, reaching 7.89 μM after 10 min in the 60 °C/Fe(III)/PDS system, suggesting the possible involvement of Fe(IV)=O (Fig. 4b). It should be noted that $PMSO_2$ formation is not definitive proof of Fe(IV)=O [54]. Therefore, the PMSO results are interpreted as suggestive but not conclusive evidence for Fe (IV)=O formation, while the radical pathways (•OH and $SO_4^{\bullet-}$) remain the dominant contributors to DIF degradation. Similarly, $PMSO_2$ was generated at pH 6.5, albeit at a lower concentration of 2.39 μM. This phenomenon is consistent with the scavenging and EPR results, indicating that Fe(III) predominantly exists in non-soluble forms under circumneutral conditions, which limits its participation in redox-mediated reactions. As noted by Pignatello et al., the activity of Fe(III)-catalyzed Fenton reactions peaks at pH 3 and diminishes as Fe(III) precipitates into amorphous iron oxyhydroxides with lower reactivity [23]. By circumneutral pH, this inert form becomes dominant, explaining the decreased activity of the heat/Fe(III)/PDS system at pH 6.5. In summary, the degradation of DIF in the heat/Fe(III)/PDS system is primarily driven by radical pathways (e.g. •OH and $SO_4^{\bullet-}$), with a possible but minor contribution from Fe(IV)=O.

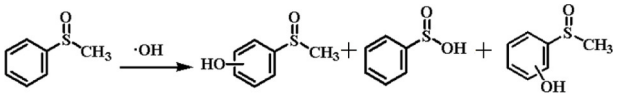

(6)

3.3.3. Analysis of complexation efficacy and electron transfer

The complexation between organic pollutants and metal ions can influence AOPs through mediated electron transfer mechanisms [23, 55]. Under ambient temperature and at pH 3.5, the absorption spectrum of the mixture containing Fe(III) and DIF exhibits substantial alterations compared to individual components, as illustrated in Fig. 4c. The observed increase in absorbance and the concomitant red shift confirm the formation of the $Fe(DIF^{\pm})^{3+}$ complexes. Previous literature suggests that the structural modifications resulting from Fe(III)-organic complexation can enhance the performance of oxidation systems through three primary pathways. First, complexation modulates the standard reduction potential of the Fe(III)/Fe(II) couple, thereby lowering the energy barrier for the reduction of Fe(III) to Fe(II). This acceleration of the rate-limiting step facilitates the efficient activation of

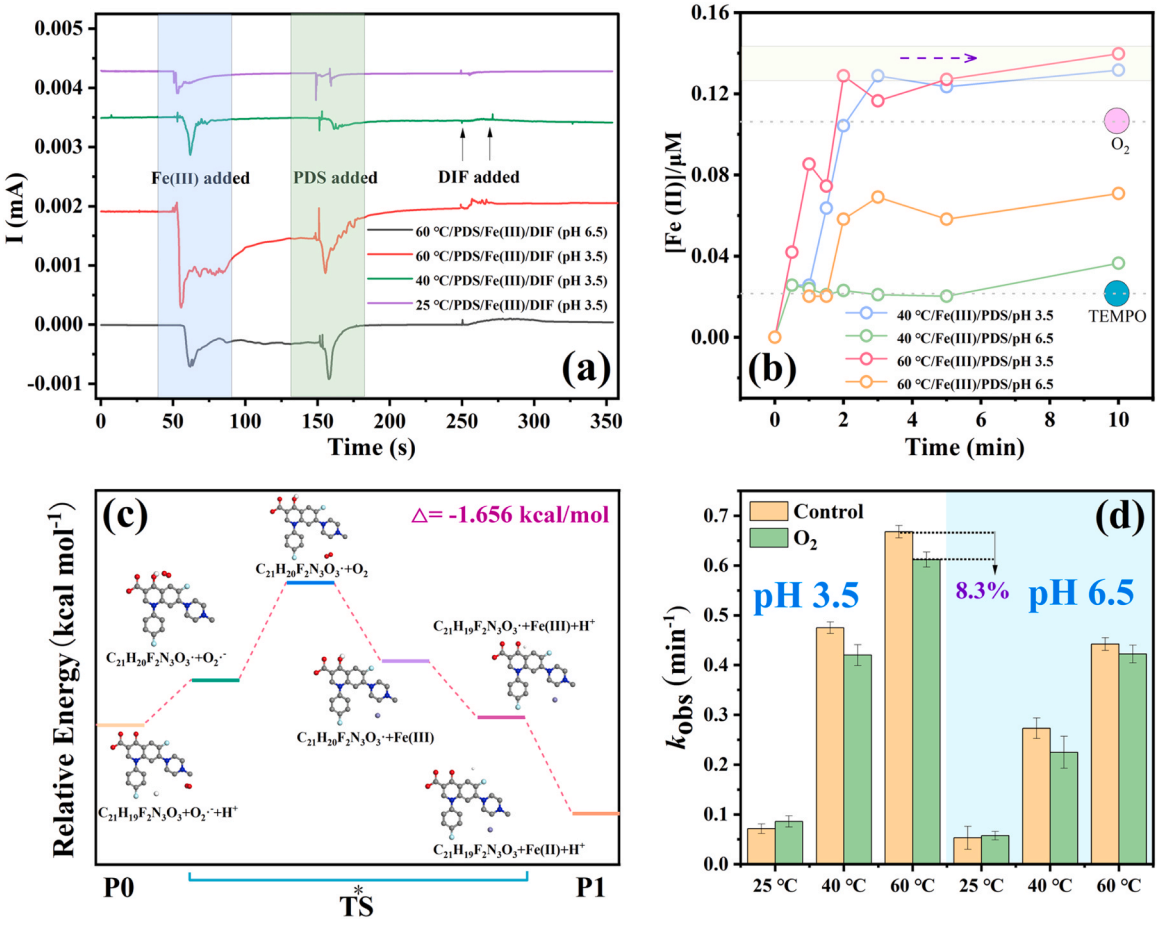

Fig. 5. Electron transfer and Fe(II) regeneration in the heat/Fe(III)/PDS system, (a) chronoamperometry (I-t) curves under different temperatures and pH conditions (electrolyte = 50 mM Na_2SO_4), (b) comparison of Fe(II) generation under different conditions; (c) Calculation and analysis of Gibbs free energy changes for Eqs. 10–11; (d) Effect of O_2 sparging on DIF degradation under different pH and temperature conditions.

PDS by Fe(II) and the subsequent generation of additional $SO_4^{\bullet-}$. Second, the formation of these complexes can shift the reaction pathways toward the induced generation of high-valent iron species such as Fe(IV)=O. These non-radical active species possess superior oxidative selectivity toward specific contaminants and demonstrate enhanced resistance to matrix interference [56]. Third, complexes enhance the *Lewis* acidity of the Fe(III) center, which enables more effective polarization of the peroxy bond in PDS. This effect weakens the O-O bond energy, as supported by theoretical calculations, making the bond more susceptible to cleavage under thermal perturbation and directly promoting PDS decomposition into reactive species [57,58].

To validate the proposed complexes-dependent mechanism, competitive experiments were conducted using the strong chelating agent EDTA. Given the exceptionally high stability constant of the Fe (III)-EDTA complexes ($log\ K = 27.51$), EDTA preferentially coordinates with Fe(III) within the system [59]. As illustrated in Fig. 4d, the addition of EDTA to the heat/Fe(III)/PDS system resulted in a significant inhibition of DIF degradation at both pH 3.5 and pH 6.5, with degradation rate reductions of 66.7% and 70.3%, respectively. This phenomenon suggests that the competitive sequestration of Fe(III) by EDTA disrupts the original $Fe(DIF^{\pm})^{3+}$ complexes structure [59]. Consequently, the three previously hypothesized enhancement pathways, including the modulation of standard potentials, the generation of Fe(IV)=O, and the intensification of *Lewis* acidity, are rendered ineffective. These results provide preliminary evidence for the pivotal role of the $Fe(DIF^{\pm})^{3+}$ complexes in PDS activation and the subsequent degradation of DIF.

Further investigation of the variations in electron transfer efficiency following complexation, which serves as the core process underlying the three aforementioned mechanisms, chronoamperometry experiments were conducted. Regardless of whether the process is mediated by free radicals or Fe(IV)=O, the fundamental essence involves electron transfer driven by the Fe(III)/Fe(II) cycle. The electrochemical results clearly demonstrate the temperature and pH dependence of the electron transfer processes within the heat/Fe(III)/PDS system (Fig. 5a). At pH 3.5, as the temperature increases from 25 ℃ to 40 ℃ and 60 ℃, distinct current response variations are observed following the sequential addition of Fe(III), PDS, and DIF. These observations indicate the occurrence of significant redox reactions and electron transfer processes. Besides, the current response is minimal at a room temperature of 25 ℃ but increases progressively with rising temperatures. The most pronounced response occurs at 60 ℃, which aligns closely with the optimal degradation kinetics observed under these conditions, confirming that elevated temperatures effectively facilitate the Fe(III)/Fe(II) valence cycle and the PDS activation process. Conversely, at pH 6.5 and 60 ℃, the current response is substantially weaker than at pH 3.5. Collectively, these complexation and electrochemical phenomena indicate that the high efficiency of the heat/Fe(III)/PDS system stems from temperature-accelerated Fe(III)/Fe(II) valence cycling [60,61]. Furthermore, an acidic environment maintains the solubility and reactivity of Fe(III). These factors synergistically enhance the electron transfer efficiency within the system, thereby driving rapid PDS activation and DIF degradation.

Compared to the standalone heat/PDS system, the introduction of Fe (III) mediates the generation and transformation of reactive species, with the valence state transition serving as the primary internal driver. To further validate this redox dual channel mechanism, the conversion

Table 1
Steady-state concentrations of •OH and $SO_4^{\bullet-}$ in different systems.

Temperature (℃)	$[•OH]_{ss}$/M		$[O_2^{\bullet-}]_{ss}$/M		$[SO_4^{\bullet-}]_{ss}$/M	
	heat/Fe(III) /PDS	heat/PDS	heat/Fe(III) /PDS	heat/PDS	heat/Fe(III) /PDS	heat/PDS
25 ℃	9.37×10^{-13}	6.92×10^{-13}	—	—	2.76×10^{-12}	6.04×10^{-13}
40 ℃	1.65×10^{-12}	1.68×10^{-12}	2.98×10^{-5}	1.45×10^{-5}	1.08×10^{-12}	7.45×10^{-12}
60 ℃	4.16×10^{-12}	2.10×10^{-12}	9.18×10^{-5}	2.75×10^{-5}	0.41×10^{-12}	9.32×10^{-12}

of Fe(III) to Fe(II) during the degradation process was monitored. As shown in Fig. 5b, the highest Fe(II) generation of 0.140 μM occurs in the heat/Fe(III)/PDS system at pH 3.5 and 60 ℃. This peak concentration matches the observation of maximum electron transfer activity in the electrochemical experiments, directly confirming that high temperature and acidic conditions synergistically accelerate the Fe(III)/Fe(II) cycle, PDS activation, and the subsequent degradation of the target pollutant [62,63].

3.3.4. Quantification of reactive species and interpretation of the multi-component synergistic oxidation network

The quantitative results from probe experiments (Table 1) provide critical evidence for the unique regulatory role of Fe(III) within the heat/PDS system. At 25 °C, the introduction of Fe(III) increased the steady-state concentration of $[•OH]_{ss}$ from 6.92×10^{-13} M to 9.37×10^{-13} M. Upon increasing the temperature to 60 °C, the $[•OH]_{ss}$ in the heat/Fe(III)/PDS system reached 4.16×10^{-12} M, representing a 1.98-fold enhancement compared to the heat/PDS system alone 2.10×10^{-12} M. These data align with quenching experiments where the contribution of •OH rose from approximately 75% to over 85%, as well as with EPR observations, thereby substantiating that the synergism between Fe(III) and thermal activation promotes the targeted generation and accumulation of •OH. Simultaneously, the concentration trends of $SO_4^{\bullet-}$ reveal a more profound interactive mechanism. At 25 °C, the $SO_4^{\bullet-}$ concentration was 2.76×10^{-12} M, which is 4.6 times higher than that of the PDS system alone, indicating that Fe(III) can activate PDS to generate $SO_4^{\bullet-}$ even at ambient temperature. However, when the temperature reached 60 ℃, $SO_4^{\bullet-}$ plummeted to 0.41×10^{-12} M, a value substantially lower than the 9.32×10^{-12} M observed in the heat/PDS system. This phenomenon is highly consistent with laser flash photolysis results, which showed a decay of the characteristic $SO_4^{\bullet-}$ absorption peak with increasing temperature, confirming that elevated temperatures accelerate the consumption and transformation of $SO_4^{\bullet-}$ in the presence of Fe(III). Given the complexity of the reactive species and their potential interconversions, fully elucidating the multi-component synergistic oxidation network presents a challenge. It is essential to clarify that thermal activation promotes the forward progression of various reactions, thereby accelerating reaction rates and modifying the steady-state concentrations of active species.

The efficient generation of $O_2^{\bullet-}$ in the heat/Fe(III)/PDS system serves as the central clue for understanding this complex oxidation network. EPR analysis (Fig. 3a) indicated that the heat/PDS system alone at 60 ℃ produced only a weak $O_2^{\bullet-}$ signal. With the addition of Fe(III), the $O_2^{\bullet-}$ signal intensity increased significantly, reaching 9.18×10^{-5} M at 60 ℃ (Table 1), which is 3.3 times that of the heat/PDS system under identical conditions. This enhancement suggests that Fe(III) initiates novel pathways for $O_2^{\bullet-}$ production [64–66]. As shown in *Eq. 7*, $O_2^{\bullet-}$ can be formed through PDS hydrolysis. Furthermore, Fe(III) reacts with PDS to produce minor amounts of Fe(II), which subsequently activates PDS or reacts rapidly with dissolved oxygen. This latter interaction, occurring via the reversible process in Eq. 8, continuously generates $O_2^{\bullet-}$ while regenerating Fe(III) [67]. Thermal energy accelerates both pathways, facilitating the substantial accumulation of $O_2^{\bullet-}$.

Although the oxidative capacity of $O_2^{\bullet-}$ is inherently weaker than that of •OH and $SO_4^{\bullet-}$ [13], its functional role within the system extends far beyond direct oxidation. Quenching experiments revealed that the addition of the $O_2^{\bullet-}$ scavenger TEMPO to the heat/PDS system reduced the DIF degradation rate by approximately 50% within 5 min (Fig. S5b). In contrast, the inhibitory effect was more pronounced in the heat/Fe(III)/PDS system, where the addition of TEMPO led to a decrease in DIF degradation of approximately 60–78% (Figs. 4a and S6). This marked enhancement in the inhibitory response suggests that, in the presence of Fe(III), $O_2^{\bullet-}$ acts as more than a secondary oxidant directly attacking DIF. More critically, it likely amplifies its indirect contribution by mediating essential redox reactions.

In conjunction with Eq. 9–*11*, the core mechanism is elucidated, identifying $O_2^{\bullet-}$ as a highly efficient reducing agent that drives Fe(II) regeneration via two distinct pathways. In the first pathway, $O_2^{\bullet-}$ directly reduces Fe(III) to produce Fe(II) as shown in the forward reaction of Eq. 9. In the second pathway, $O_2^{\bullet-}$ reacts with DIF to generate the organic radical $DIF^{\bullet-}$ (Eq. 10), an evolution process thoroughly verified in our previous discussion [7,8]. Subsequently, $DIF^{\bullet-}$ transfers electrons to Fe(III) (Eq. 11), thereby indirectly promoting Fe(II) regeneration. To verify the feasibility of the reactions depicted in Eqs. 10–11, DFT calculations were performed. The analysis of Gibbs free energy changes in Fig. 5c indicates that $\Delta G < 0$ for the system following the reaction. This confirms that the transformation of $DIF^{\bullet-}$ and Fe(III) into final products is a spontaneous process, rendering the reaction thermodynamically favorable. Moreover, the addition of TEMPO to scavenge $O_2^{\bullet-}$ inhibits both Fe(II) regeneration pathway. This results in a significant 84.8% reduction in Fe(II) concentration as illustrated in Fig. 5b. Consequently, all high-efficiency oxidative pathways activated by Fe(II) are obstructed. These include the activation of PDS by Fe(II) to generate $SO_4^{\bullet-}$ and Fe(IV)=O (Eqs. 12–13*) and* the subsequent hydrolysis of $SO_4^{\bullet-}$ under heating to produce •OH. Existing literature also suggests that Fe(IV)=O reacts with water to generate H_2O_2, which further produces •OH during Fe(II) activation. This sequence explains why the addition of Fe(III) enhances •OH production. Because the quenching of $O_2^{\bullet-}$ leads to an insufficient supply of Fe(II) as the primary engine, the entire multi-component oxidation network centered on the Fe(III)/Fe(II) cycle collapses. This explains why the ternary system exhibits a more pronounced inhibition of DIF degradation compared to the binary system upon $O_2^{\bullet-}$ quenching.

Oxygen aeration experiments further support these analytical results. As shown in Fig. 5d, apart from the negligible change at room temperature, oxygen aeration inhibits DIF degradation under various heating and pH conditions. Specifically, at pH 3.5 and 60 ℃, continuous O_2 aeration into the heat/Fe(III)/PDS system results in an 8.3% decrease in the 5-minute rate constant [26]. The introduction of excess O_2 disrupts the original equilibrium of Eq. 9 by pushing it to the left, which accelerates the conversion of Fe(II) back to Fe(III) and leads to a lower steady-state concentration of Fe(II) as confirmed in Fig. 5b.

In summary, besides direct DIF oxidation, $O_2^{\bullet-}$ serves as a key reducing agent in the heat/Fe(III)/PDS system. It regenerates Fe(II) via two pathways: Direct reduction of Fe(III) and $DIF^{\bullet-}$ mediation (Eq. 9–*11*). PDS, $SO_4^{\bullet-}$, Fe(IV)=O, and •OH drive the oxidative terminal (Eqs. 12–15*)*, forming a Fe(III)/Fe(II)-centered redox dual-channel network. Thus, the Fe(III)/Fe(II) cycle mediates the generation and transformation of reactive species in the heat/PDS system, where multiple reactive species work in concert to achieve high-efficiency DIF degradation (Eq. 16). This multi-oxidant synergy (•OH, $SO_4^{\bullet-}$, Fe(IV)=O and $O_2^{\bullet-}$) explains why the system (k_{obs} = 0.668 min^{-1}) outperforms

heat/PDS (k_{obs} = 0.219 min^{-1}) despite only twice the •OH level.

$$2S_2O_8^{2-} + 2H_2O \xrightarrow{heat} SO_4^{\bullet-} + O_2^{\bullet-} + 4H^+ + 3SO_4^{2-} \quad (7)$$

$$Fe(III) + S_2O_8^{2-} \xrightarrow{heat} S_2O_8^{\bullet-} + Fe(II), k = (2.8-6) \times 10^{-6} M^{-1}S^{-1} \quad (8)$$

$$O_2^{\bullet-} + Fe(III) \xrightarrow{heat} Fe(II) + O_2, k = 1.5 \times 10^{-8} M^{-1}S^{-1} \quad (9)$$

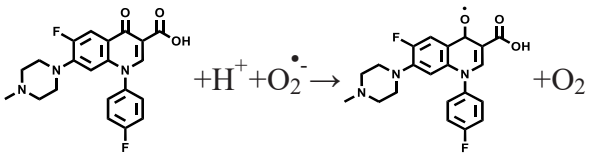

(10)

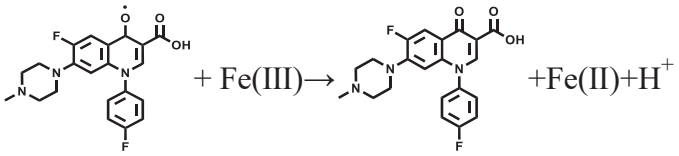

(11)

$$Fe(II) + S_2O_8^{2-} \xrightarrow{heat} SO_4^{\bullet-} + Fe(III) + SO_4^{2-} \quad (12)$$

$$Fe(II) + S_2O_8^{2-} + H_2O \xrightarrow{heat} Fe^{IV}O^{2+} + 2SO_4^{2-} + 2H^+ \quad (13)$$

$$Fe(II) + SO_4^{\bullet-} \xrightarrow{heat} Fe(III) + SO_4^{2-}, k = 4.6 \times 10^9 M^{-1}\ S^{-1} \quad (14)$$

$$Fe^{IV}O^{2+} + Fe(II) + 2H^+ \xrightarrow{heat} 2Fe(III) + H_2O \quad (15)$$

$$\bullet OH \Big/ SO_4^{\bullet-} \Big/ Fe^{IV}O^{2+} \Big/ O_2^{\bullet-} + DIF \rightarrow products \quad (16)$$

3.4. Efficacy of heat/PDS systems mediated by diverse metal ions

The activation efficacy of various metal ions (Co(II), Mn(II), Cr(III)) for PDS in DIF degradation is collaboratively regulated by pH and temperature. At 25 ℃, most metal ions showed weak activation at pH 3.5, while at pH 6.5, only Mn(II) exhibited a slight promotional effect (Fig. S7a-b). As temperature increased to 40 ℃, Fe(III) and Mn(II) at pH 3.5 enhanced DIF degradation by approximately 23% and 4% within 20 min, respectively, compared to heat/PDS alone. At pH 6.5, all tested metal ions outperformed thermal activation alone, with Co(II) boosting the degradation rate by ~21% (Fig. S7c-d). At 60 ℃, Fe(III) remained the most effective at pH 3.5, whereas at pH 6.5, Mn(II), Co(II), and Fe (III) all markedly accelerated degradation, with increments of 7.8–11.3% (Fig. S7e-f).

Therefore, except for Fe(III) which tends to form insoluble species at near-neutral pH, circumneutral conditions (pH 6.5) are generally more favorable for the activated functions of Mn(II) and Co(II), aligning with our previous findings on Cu(II) and other studies [68,69]. For Mn(II), the promotional effect is attributed to the formation of an electronic bridge with pollutants under circumneutral conditions, enhancing its electron density and facilitating PDS activation [68]. In contrast, Cr(III) exhibited weak activation across all conditions due to its inherent inertness in activating oxidants.

To explore the intrinsic correlation between metal-ion properties and activation performance, the correlation between the first hydrolysis constant (pK_a) and standard potential (E^0) of various metal ions with the DIF degradation rate constant (k) was analyzed (Table 2, Fig. 6). A negative correlation was observed between pK_a and k (Fig. 6a), particularly at pH 3.5, where metal ions with lower pK_a (e.g., Fe(III)) exist as free hydrated ions, facilitating complexation and electron transfer. Regarding E^o, a general negative correlation with activation efficiency was found (Fig. 6b). Metal ions with lower standard potentials (e.g., Fe (III)) undergo valence cycling more easily. However, Cu(II) exhibited exceptional activity at circumneutral pH despite its relatively high potential, indicating that electrode potential alone does not determine activation performance. These findings confirm that the mediating capacity of metal ions in heat/PDS systems is governed by a multifactorial framework involving solution speciation, valence cycling kinetics, and pH adaptability, rather than standard potentials alone [78–80]. Among the ions tested, Fe(III) is distinctive in that it achieves high efficiency under acidic conditions (pH 3.5) and already at low temperature (40 °C), highlighting its unique advantage for low-carbon water treatment. This systematic comparison provides essential guidance for selecting tailored PDS activation strategies for specific water quality characteristics.

Table 2
Correlation analysis between the standard redox potential of different metal ions and their rate constants for DIF degradation in the heat/PDS system (conditions: [PDS] = 2 mM, [Metalion] = 17.9 μM, [DIF] = 10 mg/L, error bars represent standard deviation).

Redox couple	pK_a	E^0 (V)	pH 3.5 (k/min^{-1})			pH 6.5 (k/min^{-1})		
			25 ℃	40 ℃	60 ℃	25 ℃	40 ℃	60 ℃
Cr(III)/Cr(VI)	4.6	1.35	0.005	0.039	0.142	0.005	0.054	0.199
Mn(II)/Mn(III)	10.6	1.51	0.005	0.062	0.167	0.006	0.078	0.283
Co(II)/Co(III)	9.3	1.81	0.006	0.050	0.197	0.005	0.093	0.304
Fe(III)/Fe(II)	3.0	0.77	0.071	0.475	0.678	0.053	0.273	0.442
Cu(II)/Cu(III)	7.6	1.57	0.016	0.031	0.451	0.041	0.151	0.694

Note that the pK_a values in the figure correspond to the transformation of metal ions into $MOH^{(n-1)+}$ species. Due to the complexity and significant variability of hydrolysis processes, only the first hydrolysis pK_a is recorded [27,70–73]. The half-reactions for the Mn(II)/Mn(III), Co(II)/Co(III), Fe(III)/Fe(II) and Cu(II)/Cu(III) redox couples do not involve proton transfer, and thus their standard potentials [28,74–77] are utilized directly for comparisons across different pH levels. Although the Cr(III)/Cr(VI) potential is pH-dependent, literature values are consistently employed to maintain data uniformity during correlation analysis.

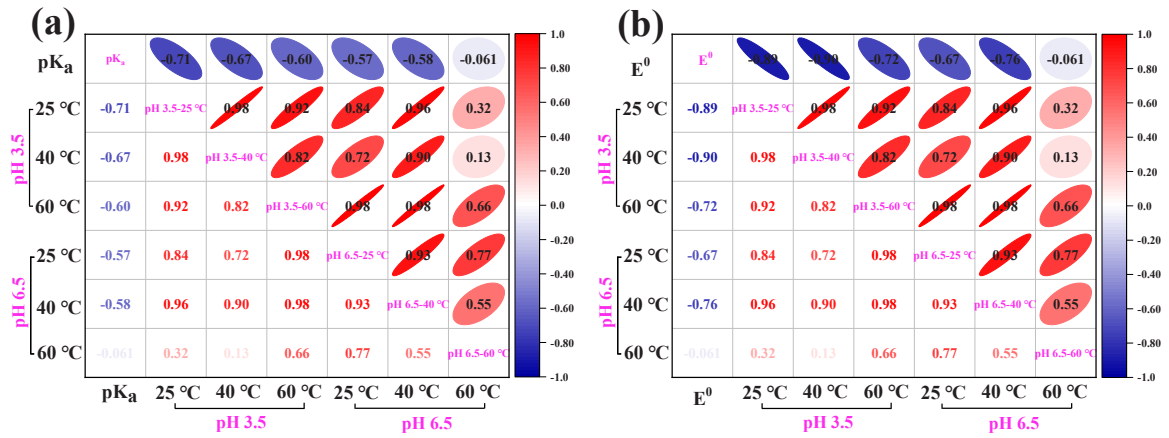

Fig. 6. Correlation analysis between the DIF degradation rate constant and (a) the first hydrolysis pK_a and (b) the standard potential of different metal ions.

4. Conclusions

This study systematically elucidates the core principle by which Fe (III) establishes a redox dual channel mechanism in the thermally activated PDS system. The synergistic effect between Fe(III) and heat is markedly triggered at 40 ℃, enhancing the DIF degradation rate constant by 20.30-fold and 5.67-fold over the heat/PDS and Fe(III)/PDS systems alone, respectively, highlighting a low-temperature activation advantage. This synergy arises from Fe(III)-mediated reduction of E_a from 89.58 to 18.53 kJ/mol. At 60 ℃, a temperature achievable with industrial waste heat or solar thermal collection, the system achieves faster kinetics and robust performance. The •OH steady-state concentration reaches 4.16×10^{-12} M (1.98 times that of heat/PDS), and the multi-oxidant synergy (•OH, $SO_4^{\bullet-}$, Fe(IV)=O, and $O_2^{\bullet-}$) ensures efficient degradation in real water matrices. Mechanistic investigations reveal that Fe(III) forms $Fe(DIF^{\pm})^{3+}$ complexes with DIF, which facilitate interfacial electron transfer and accelerates the Fe(III)/Fe(II) valence cycle. Within this cycle, two channels operate simultaneously. The oxidative channel, driven by PDS and $SO_4^{\bullet-}$, converts Fe(II) to Fe(III) and contributes to Fe(IV)=O generation, whereas the reductive channel, mediated by $O_2^{\bullet-}$, promotes Fe(II) regeneration via direct Fe(III) reduction and formation of $DIF^{\bullet-}$. The two channels operate in concert to sustain the valence cycle and establish a multi-component synergistic oxidation network. System reactivity is strongly pH-dependent. Under acidic conditions, Fe(III) remains in soluble forms conducive to the reaction, and the multi-oxidant synergy enhances robustness against water matrix interference. This study provides theoretical foundation and technical pathway for leveraging environmentally abundant iron ions in conjunction with low-grade thermal energy to achieve efficient, low-carbon purification of antibiotic-contaminated wastewater.

Environmental implication

Fluoroquinolone pollution poses significant ecological risks. While thermally activated persulfate is effective, high-energy costs hinder its application. This study introduces an Fe(III)-mediated redox dual-channel mechanism that dramatically lowers the activation energy from 89.58 to 18.53 kJ/mol. By leveraging $O_2^{\bullet-}$-driven iron cycling to synchronize oxidative and reductive pathways, the system achieves superior performance at mild temperatures (40–60 ℃). This provides a low-carbon, sustainable strategy for antibiotic remediation by utilizing ubiquitous iron ions and low-grade industrial waste heat.

CRediT authorship contribution statement

Yanli Wang: Resources, Methodology, Formal analysis. **Zheng Hu:** Validation, Methodology. **Yongpeng Zhang:** Software, Resources, Methodology, Formal analysis. **Ping Chen:** Writing – review & editing, Supervision, Funding acquisition, Conceptualization. **Lingzhi Shen:** Writing – review & editing, Software, Methodology, Investigation, Data curation. **Zhenjun Xiao:** Software, Methodology, Data curation. **Zihong Xu:** Validation, Resources, Methodology. **Guoguang Liu:** Writing – review & editing, Supervision, Funding acquisition. **Yuxing Xian:** Software, Resources, Methodology, Formal analysis, Data curation. **Wenying Lv:** Writing – review & editing, Supervision, Funding acquisition. **Yixun Zheng:** Validation, Resources, Methodology. **Zihao Guo:** Validation, Methodology. **Zili Lin:** Writing – review & editing, Methodology. **Yue Yang:** Validation, Resources, Methodology. **Kun Yao:** Writing – review & editing, Supervision, Conceptualization.

Declaration of Competing Interest

The authors declare that they have no known competing financial interests or personal relationships that could have appeared to influence the work reported in this paper.

Acknowledgements

This work was supported by the National Natural Science Foundation of China [No. 21906029, 22076029 and 22176042], the Natural Science Foundation Project of Guangdong Province of China [No. 2024A1515011742 and 2025A1515012104]. The authors thank the Analysis and Test Center of Guangdong University of Technology for performing the laser flash photolysis measurements.

Appendix A. Supporting information

Supplementary data associated with this article can be found in the online version at doi:10.1016/j.jhazmat.2026.142782.

Data availability

Data will be made available on request.

References

[1] Wen, L., Dai, J., Song, J., et al., 2025. Unveiling the characteristics of fluoroquinolones in China marginal seas: spatiotemporal distribution, environmental fate, and mass inventory. Mar Pollut Bull 218, 118161.
[2] Masud, M.A.A., Shin, W.S., Septian, A., et al., 2024. Exploring the environmental pathways and challenges of fluoroquinolone antibiotics: a state-of-the-art review. Sci Total Environ 926, 171944.
[3] Wang, C., Du, J., Liang, Z., et al., 2022. High-efficiency oxidation of fluoroquinolones by the synergistic activation of peroxymonosulfate via vacuum ultraviolet and ferrous iron. J Hazard Mater 422, 126884.

[4] Sadek, A.H.S., Xu, A., Hassan, G.K., et al., 2026. Transformation and detoxification of fluoroquinolone antibiotics by singlet oxygen: a review. Sep Purif Technol 380, 135279.
[5] Lu, J., Wu, J., Zhang, C., et al., 2018. Occurrence, distribution, and ecological-health risks of selected antibiotics in coastal waters along the coastline of China. Sci Total Environ 644, 1469–1476.
[6] Ben, W., Zhu, B., Yuan, X., et al., 2018. Occurrence, removal and risk of organic micropollutants in wastewater treatment plants across China: comparison of wastewater treatment processes. Water Res 130, 38–46.
[7] Shen, L., Xu, Z., Xiao, Z., et al., 2025. Insight into the degradation of difloxacin by heat/persulfate system: mechanism, pathway and application. Sep Purif Technol 362, 131661.
[8] Neta, P., Huie, R.E., Ross, A.B., 1988. Rate constants for reactions of inorganic radicals in aqueous solution. J Phys Chem Ref Data 17 (3), 1027–1284.
[9] Wang, C., Liu, X., Yang, Y., et al., 2021. Antibiotic and antibiotic resistance genes in freshwater aquaculture ponds in China: a meta-analysis and assessment. J Clean Prod 329, 129719.
[10] Zheng, D., Yin, G., Liu, M., et al., 2021. A systematic review of antibiotics and antibiotic resistance genes in estuarine and coastal environments. Sci Total Environ 777, 146009.
[11] Wilkinson, J.L., Boxall, A.B.A., Kolpin, D.W., et al., 2022. Pharmaceutical pollution of the world's rivers [J. Proc Natl Acad Sci 119 (8), e2113947119.
[12] Zhang, D., Li, Y., Wang, P., et al., 2023. Dynamic active-site induced by host-guest interactions boost the Fenton-like reaction for organic wastewater treatment. Nat Commun 14 (1), 3538.
[13] Wang, J., Wang, S., 2020. Reactive species in advanced oxidation processes: formation, identification and reaction mechanism. Chem Eng J 401, 126158.
[14] Ali, J., Shahzad, A., Wang, J., et al., 2021. Modulating the redox cycles of homogenous Fe(III)/PMS system through constructing electron rich thiomolybdate centres in confined layered double hydroxides. Chem Eng J 408, 127242.
[15] Li, N., Wu, S., Dai, H., et al., 2022. Thermal activation of persulfates for organic wastewater purification: heating modes, mechanism and influencing factors. Chem Eng J 450, 137976.
[16] Senthilkumar, A., Ganeshbabu, M., Karuppiah Lazarus, J., et al., 2023. Thermal and radiation based catalytic activation of persulfate systems in the removal of micropollutants: a review. Ind & Eng Chem Res 62 (11), 4554–4572.
[17] Ren, W., Huang, X., Wang, L., et al., 2021. Degradation of simazine by heat-activated peroxydisulfate process: a coherent study on kinetics, radicals and models. Chem Eng J 426, 131876.
[18] Heikkinen, K., Saari, M., Heino, J., et al., 2022. Iron in boreal river catchments: biogeochemical, ecological and management implications. Sci Total Environ 805, 150256.
[19] Chen, L., Ma, T., Wang, Y., et al., 2020. Health risks associated with multiple metal (loid)s in groundwater: a case study at Hetao Plain, northern China. Environ Pollut 263, 114562.
[20] Xia, X., Teng, Y., Zhai, Y., 2022. Biogeochemistry of iron enrichment in groundwater: an indicator of environmental pollution and its management. Sustainability 14 (12), 7059.
[21] Somero, G.N., 2002. Thermal physiology and vertical zonation of intertidal animals: optima, limits, and costs of living. Integr Comp Biol 42 (4), 780–789.
[22] Li, Y., He, B., Lin, J., et al., 2025. Efficient polymerization removal of phenolic pollutants by in situ-formed iron-complexes in thermally activated peroxydisulfate systems. Environ Sci Technol 59 (30), 16001–16010.
[23] Pignatello, J.J., Oliveros, E., Mackay, A., 2006. Advanced oxidation processes for organic contaminant destruction based on the Fenton reaction and related chemistry. Crit Rev Environ Sci Technol 36 (1), 1–84.
[24] Cai, C., Lin, Y., Xie, X., et al., 2025. New insights into selective degradation of organic contaminants by Fe^{3+}/persulfate process: performance, mechanism, and theoretical calculations. Sep Purif Technol 354, 128773.
[25] Merouani, S., Stanbouli, O., Ziadi, I., et al., 2026. Semi-pilot scale implementation of Fe(II)/chlorine process for textile dyes mineralization: comparative assessment with Fenton and Fe(II)/persulfate systems. Sep Purif Technol 382, 135511.
[26] Shen, L., Chen, K., Zheng, Y., et al., 2025. Highly synergistic decontamination of fluoroquinolone antibiotics via thermally-switchable radicals in Cu(II)/PDS system. J Hazard Mater 499, 140230.
[27] Rickard, D., 2012. Chapter 3-sedimentary iron biogeochemistry [M]//RICKARD D. Developments in Sedimentology. Elsevier, pp. 85–119.
[28] Popova, T.V., Aksenova, N.V., 2003. Complexes of copper in unstable oxidation states. Russ J Coord Chem 29 (11), 743–765.
[29] Shu, Z., Pan, Z., Wang, X., et al., 2022. Sunlight-induced interfacial electron transfer of ferrihydrite under oxic conditions: mineral transformation and redox active species production. Environ Sci & Technol 56 (19), 14188–14197.
[30] Zhou, Y., Lei, Y., Kong, Q., et al., 2023. Reactions of neonicotinoids with peroxydisulfate: the generation of neonicotinoid anion radicals and activation pathway to form sulfate radicals. J Hazard Mater 450, 131081.
[31] Ren, W., Cheng, C., Shao, P., et al., 2022. Origins of electron-transfer regime in persulfate-based nonradical oxidation processes. Environ Sci Technol 56 (1), 78–97.
[32] Yang, Y., Banerjee, G., Brudvig, G.W., et al., 2018. Oxidation of organic compounds in water by unactivated peroxymonosulfate. Environ Sci Technol 52 (10), 5911–5919.
[33] Olojo, R.O., Xia, R.H., Abramson, J.J., 2005. Spectrophotometric and fluorometric assay of superoxide ion using 4-chloro-7-nitrobenzo-2-oxa-1,3-diazole. Anal Biochem 339 (2), 338–344.
[34] Tang, Y., Dou, J., Lu, Z., et al., 2023. Accelerating Fe^{2+}/Fe^{3+} cycle via biochar to improve catalytic degradation efficiency of the Fe^{3+}/persulfate oxidation. Environ Pollut 316, 120669.
[35] Perdew, J.P., Burke, K., Ernzerhof, M., 1996. Generalized gradient approximation made simple. Phys Rev Lett 77 (18), 3865.
[36] Perdew, J.P., 1991. Generalized gradient approximations for exchange and correlation: a look backward and forward. Phys B Condens Matter 172 (1-2), 1–6.
[37] Wang, Y., Xiao, Z., et al., 2024. Concentrated solar energy-driven photothermal efficient degradation and mineralization of fluoroquinolone antibiotics in various water bodies. Chem Eng J 501, 157739.
[38] Chen, P., Blaney, L., Cagnetta, G., et al., 2019. Degradation of ofloxacin by perylene diimide supramolecular nanofiber sunlight-driven photocatalysis. Environ Sci Technol 53 (3), 1564–1575.
[39] Yuan, Z., Cui, J., Gao, S., et al., 2025. Synergistic effect on accelerated Fe(III)/Fe(II) cycle and enhanced piezoelectric field for PDS activation of ofloxacin degradation. Chem Eng J 524, 169436.
[40] Miu, K., Meng, Y., Yan, Y., et al., 2025. Quantitative profiling of elementary reaction steps in sulfate radical-based treatment processes: a two-loop self-consistent approach. Environ Sci Technol 59 (29), 15457–15467.
[41] Pang, S.-C., Huang, N., Chen, Q.-Y., et al., 2025. The impact of chloride and nitrogenous ions on advanced oxidation processes: radical formation, pollutant removal, transformation products, and toxicity changes. J Environ Chem Eng 13 (5), 117795.
[42] Chen, C., Wu, Z., Hou, S., et al., 2022. Transformation of gemfibrozil by the interaction of chloride with sulfate radicals: radical chemistry, transient intermediates and pathways. Water Res 209, 117944.
[43] Zheng, Y., Yang, Y., Wang, Y., et al., 2025. Construction of a novel concentrated sunlight/PDS system for efficient remediation of methyl parathion-polluted water: synergistic photothermal activation and phosphorus fate mechanisms. Chem Eng J 525, 170219.
[44] He, X., Pelaez, M., Westrick, J.A., et al., 2012. Efficient removal of microcystin-LR by UV-C/H_2O_2 in synthetic and natural water samples. Water Res 46 (5), 1501–1510.
[45] Yang, P., Chu, H., Liu, J., et al., 2025. Nitrite leads to the formation of N-nitrosodimethylamine during sulfate radical oxidation of dimethylamine compounds. Water Res 271, 122879.
[46] Chen, C., Wu, Z., Hua, Z., et al., 2021. Mechanistic and kinetic understanding of micropollutant degradation by the UV/NH2Cl process in simulated drinking water. Water Res 204, 117569.
[47] Wu, L., Ong, W.L., Ho, G.W., 2025. Advancing seawater electrochemical reaction for fuel and chemical production. ACS Nano 19 (11), 10779–10795.
[48] Zhai, L., Li, F., He, Y., et al., 2023. Degradation of norfloxacin by sulfur-doped iron-cobalt oxides activated perodisulfate: synergism between free radicals and singlet oxygen. Chem Eng J 478, 147378.
[49] Meng, S., Zhou, P., Sun, Y., et al., 2022. Reducing agents enhanced Fenton-like oxidation (Fe(III)/Peroxydisulfate): substrate specific reactivity of reactive oxygen species. Water Res 218, 118412.
[50] Keenan, C.R., Sedlak, D.L., 2008. Ligand-enhanced reactive oxidant generation by nanoparticulate zero-valent iron and oxygen. Environ Sci Technol 42 (18), 6936–6941.
[51] Luo, Z., Yan, Y., Spinney, R., et al., 2024. Environmental implications of superoxide radicals: from natural processes to engineering applications. Water Res 261, 122023.
[52] Chen, L., Wang, S., Yang, Z., et al., 2021. Selective interfacial oxidation of organic pollutants in Fenton-like system mediated by Fe(III)-adsorbed carbon nanotubes. Appl Catal B Environ 292, 120193.
[53] Hu, K., Zhou, P., Yang, Y., et al., 2024. The nature of molecular hybridizations in nanodiamonds for boosted Fe(III)/Fe(II) circulation. Environ Sci Technol 58 (46), 20665–20675.
[54] Chen, Y., Miller, C.J., Xie, J., et al., 2023. Challenges relating to the quantification of Ferryl(IV) ion and hydroxyl radical generation rates using methyl phenyl sulfoxide (PMSO), phthalhydrazide, and benzoic acid as probe compounds in the homogeneous Fenton reaction. Environ Sci Technol 57 (47), 18617–18625.
[55] Wu, J., Bao, J., Zhang, X., et al., 2024. Synergistic effect of facet-regulated and photocatalytic-peroxymonosulfate activation of Fe(II)/decahedron monoclinic $BiVO_4$ composites for efficient degradation of tetracycline. J Clean Prod 459, 142425.
[56] Wang, S., Dong, H., Shao, B., et al., 2025. High-valent iron species (Fe(IV)/Fe(V)) for selective oxidation of emerging contaminants: mechanisms, applications, and future directions. Environ Sci Technol 59 (43), 23005–23023.
[57] Yin, R., Chen, Y., Hu, J., et al., 2021. Complexes of Fe(III)-organic pollutants that directly activate Fenton-like processes under visible light. Appl Catal B Environ 283, 119663.
[58] Duijnstee, D.R., Di Berto Mancini, M., De Roo, C.M., et al., 2025. Ligand driven heterolytic O–O bond cleavage in a non-haem phenolato-Fe(iii)–OOH complex to yield a formal Fe(v)□O intermediate. Dalton Trans 54 (38), 14566–14577.
[59] Fujii, M., Rose, A.L., Waite, T.D., et al., 2008. Effect of divalent cations on the kinetics of Fe(III) complexation by organic ligands in natural waters. Geochim Et Cosmochim Acta 72 (5), 1335–1349.
[60] Zhang, Y., Duan, Z., Jin, Y., et al., 2023. Chemical bond bridging across two domains: generation of Fe(II) and in situ formation of FeSx on zerovalent iron. Environ Sci Technol 57 (30), 11336–11344.
[61] Liu, F., Ren, H., Lin, Y., 2024. Enhanced 2,4-DCP removal by electro-Fenton process using PEDOT modified graphite felt cathode: promoting H_2O_2 generation and Fe^{3+}/Fe^{2+} cycle. J Environ Chem Eng 12 (3), 112718.

[62] Ying, Y., Liang, S., Zhang, F., et al., 2024. Accelerated Fe^{3+}/Fe^{2+} cycle in Mo_2C-based Fe catalyst to promote peroxymonosulfate activation. Chemosphere 367, 143380.
[63] Ruan, R., Jiang, B., Yuan, J., et al., 2026. Synergistic Fe-Ni/CF composite cathode facilitating Fe^{3+}/Fe^{2+} cycling and electron transfer for efficient ibuprofen degradation in MFC®EF systems. Chem Eng J 530, 173469.
[64] Melton, E.D., Swanner, E.D., Behrens, S., et al., 2014. The interplay of microbially mediated and abiotic reactions in the biogeochemical Fe cycle. Nat Rev Microbiol 12 (12), 797–808.
[65] King, D.W., Lounsbury, H.A., Millero, F.J., 1995. Rates and mechanism of Fe(II) oxidation at nanomolar total iron concentrations. Environ Sci Technol 29 (3), 818–824.
[66] Santana-Casiano, J.M., González-Dávila, M., Millero, F.J., 2005. Oxidation of nanomolar levels of Fe(II) with oxygen in natural waters. Environ Sci Technol 39 (7), 2073–2079.
[67] Zhang, S., Wei, Y., Metz, J., et al., 2022. Persistent free radicals in biochar enhance superoxide-mediated Fe(III)/Fe(II) cycling and the efficacy of CaO_2 Fenton-like treatment. J Hazard Mater 421, 126805.
[68] Gao, Y., Zhou, Y., Pang, S.-Y., et al., 2021. Enhanced peroxymonosulfate activation via complexed Mn(II): a novel non-radical oxidation mechanism involving manganese intermediates. Water Res 193, 116856.
[69] Anipsitakis, G.P., Dionysiou, D.D., 2003. Degradation of organic contaminants in water with sulfate radicals generated by the conjunction of peroxymonosulfate with cobalt. Environ Sci Technol 37 (20), 4790–4797.
[70] Wrona, P.K., 1992. Electrochemical behavior of Cr(II) and Cr(III) ions in weakly acidic solutions. J Electroanal Chem 322 (1), 119–132.
[71] Li, J., Fisher, C.L., Chen, J.L., et al., 1996. Calculation of redox potentials and pKa values of hydrated transition metal cations by a combined density functional and continuum dielectric theory. Inorg Chem 35 (16), 4694–4702.
[72] Plyasunova, N.V., Zhang, Y., Muhammed, M., 1998. Critical evaluation of thermodynamics of complex formation of metal ions in aqueous solutions. IV. Hydrolysis and hydroxo-complexes of Ni^{2+} at 298.15 K. Hydrometallurgy 48 (1), 43–63.
[73] Lu, B., Wu, J., Tang, C., et al., 2026. Facilitating redox cycles of copper species by peroxydisulfate in the copper-catalyzed Fenton-like system for enhanced oxidation of organic contaminants. Water Res 289, 124839.
[74] Dong, H., Wei, G., Cao, T., et al., 2020. Insights into the oxidation of organic cocontaminants during Cr(VI) reduction by sulfite: the overlooked significance of Cr(V). Environ Sci Technol 54 (2), 1157–1166.
[75] Lu, Y., Liu, W., Jin, Q., et al., 2025. Enhanced activation of peroxymonosulfate by introducing Co/Fe atoms in $LaCoO_3$-biochar derived catalysts for the degradation of sulfamethoxazole. Sep Purif Technol 357, 130070.
[76] Zeng, H., Cheng, Y., Repo, E., et al., 2022. Trace iron as single-electron shuttle for interdependent activation of peroxydisulfate and HSO_3^-/O_2 enables accelerated generation of radicals. Water Res 223, 118935.
[77] Yuan, W., Cai, L., Lu, L., et al., 2025. Reversible Mn^{3+}/Mn^{2+} redox chemistry for high-rate aqueous manganese-ion batteries. Energy Storage Mater 82, 104598.
[78] Wang, L., Xu, H., Jiang, N., et al., 2020. Trace cupric species triggered decomposition of peroxymonosulfate and degradation of organic pollutants: Cu(III) being the primary and selective intermediate oxidant. Environ Sci Technol 54 (7), 4686–4694.
[79] Lin, B., Liu, G., Zheng, Z., et al., 2025. Enhanced peroxymonosulfate activation by Co/Mn and P modified carbon nitride for ciprofloxacin degradation: performance, mechanism and toxicity assessment. J Environ Chem Eng 13 (3), 116604.
[80] Liang, C., Liu, X., Ling, C., et al., 2024. Proton-coupled electron transfer activation of peroxydisulfate with phosphorylated zero-valent iron. Appl Catal B Environ Energy 352, 124025.